Materials and Design 188 (2020) 108423

Contents lists available at ScienceDirect

Materials and Design

journal homepage: www.elsevier.com/locate/matdes

Experimental study and crystal plasticity finite element simulations of nano-indentation-induced lattice rotation and the underlying mechanism in TC6 single α-grain

Yu Zhou [a,b], Qunbo Fan [a,b,c,*], Xin Liu [a,b], Duoduo Wang [a,b,c], Xinjie Zhu [a,b,c]

[a] School of Materials Science and Engineering, Beijing Institute of Technology, Beijing 100081, China
[b] National Key Laboratory of Science and Technology on Materials Under Shock and Impact, Beijing 100081, China
[c] Beijing Institute of Technology Chongqing Innovation Center, Chongqing 401135, China

HIGHLIGHTS

- High-resolution orientation characterization of the severely deformed Berkovich indentation is achieved with FIB and PED.
- Simulation of lattice rotations agrees quite well with the experimental phenomenon.
- The complex generation and growth of subgrains caused by nano-indentation are successfully predicted.

GRAPHICAL ABSTRACT

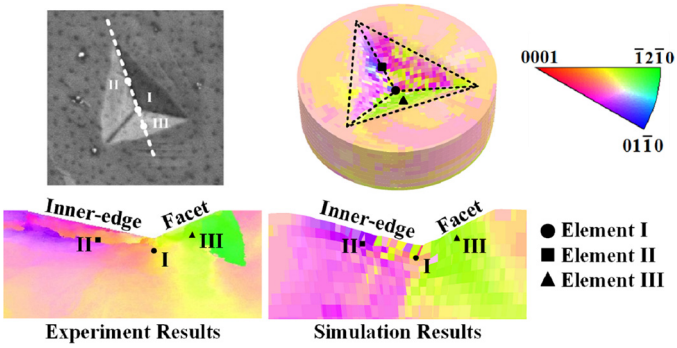

ARTICLE INFO

Article history:
Received 5 July 2019
Received in revised form 6 December 2019
Accepted 11 December 2019
Available online 13 December 2019

Keywords:
Titanium alloy
Nano-indentation
CPFEM
Lattice rotation
Plastic deformation mechanism

ABSTRACT

A Berkovich indentation test was performed in a single primary α-phase grain of an equiaxed TC6 titanium alloy, to reveal the complex local lattice-rotation process under nano-indentation loading. Numerical simulations using an in-house-developed crystal plasticity finite element method code were also conducted. A high-resolution inverse pole figure of a slice across the nano-indention was obtained via the focused ion beam technique coupled with precession electron diffraction. The simulation results corresponded closely to the experimental observations. In the slice, the region beneath the indentation inner-edge and the region beneath the indentation facet underwent the greatest degree and the second-greatest degree of lattice rotation, respectively. In contrast, for the region directly below the indentation center, the lattice rotated first, but the orientation changed only slightly during the entire process. The bright field transmission electron microscopy and the geometrically necessary dislocation densities provided experimental confirmation of such orientation features. Furthermore, the nucleation and continuous growth process of subgrains was numerically predicted by virtually tracking the misorientation angle (>10°) map at different indentation depths in three-dimensional space. Thereafter, the evolution of each slip system type was captured at typical local regions of the indentation, leading to an in-depth understanding of the underlying mechanism.

* Corresponding author at: School of Materials Science and Engineering, Beijing Institute of Technology, Beijing 100081, China.
E-mail address: fanqunbo@bit.edu.cn (Q. Fan).

https://doi.org/10.1016/j.matdes.2019.108423

1. Introduction

Owing to their high strength, low density, and high corrosion resistance, titanium alloys have a wide range of applications in the aerospace and biomedical industries as well as other fields [1,2]. These excellent mechanical properties are attributed to microstructural characteristics, such as the crystal orientation, grain size, and morphology [3–5]. Furthermore, owing to the preferred distribution of crystal orientations or lattice orientations, these alloys exhibit diverse mechanical response behaviors when subjected to different loads. Therefore, the influence of the crystal orientation on the plastic deformation mechanism and mechanical response of titanium alloys has received increasing attention. The mechanical behavior and microstructural evolution of titanium alloy materials under macroscopic loading, such as extrusion, rolling, forging, and cutting [6–9], has been extensively studied. However, studies on the orientations and mechanical responses of titanium alloys under microscopic loading are rare. Nevertheless, in recent years, important findings on the elastoplastic deformation mechanism of materials have been obtained for the microscopic length scales [10–13]. By studying the correlation between crystallographic orientations and mechanical properties of individual grains in CP-Ti, Fizanne-Michel et al. [13] found that hardness varies significantly with orientation, and that the elastic modulus appears less sensitive than hardness to grain orientation. An investigation of the mechanical response and orientation evolution of titanium alloys subjected to microscopic loading is essential for improved understanding of this mechanism.

In recent years, various micro-regional loading methods, including micro-pillar compression, in-situ tensile testing, and nano-indentation, have been developed with the aim of investigating the micromechanical response of materials. Nano-indentation testing is the most versatile of these methods, and complex loading conditions may be applied to the local micro-regions of the samples, due to the different shapes of the indenters. Nano-indentation has been used to evaluate the frictional force, strength, super-elasticity, and toughness of titanium alloys. Ehtemam-Haghighi et al. [14] studied the effect of Fe and Ta content on the microstructure of Ti-Fe-Ta alloy by assessing hardness, reduced elastic modulus, elastic recovery and wear resistance using nano-indentation. Wang et al. [15] investigated surface modification through friction stir processing method by performing nano-indentation test at different locations near the stir zone, which provides new insight into the surface modification of beta titanium alloys. In Lv's work [16], Ti6Al4V/Zn composite with various types of surface nanostructure, including nanograins, nanotwins and nano lamellae, were fabricated by friction stir processing. The mechanical response of sample surface was systematic investigated by nano-indentation, and the nanoscale deformation mechanism is discussed in detail. In addition, based on the high precision of forces and displacements, nano-indentation testing can accurately reflect the deformation resistance of the microstructures by continuously recording the displacement-load changes during the loading and unloading process. Jun et al. [17] determined the deformation mechanism of dual phase titanium alloys at different strain rates through a series of nano-indentation tests on the surface of the sample. The findings revealed that the high strain-rate sensitivity results from the lattice orientations, and is also correlated with the distribution of the β-phase. Similarly, Su et al. [18] investigated the deformation close to a number of low and high angle grain boundaries in an α-phase titanium alloy by assessing the topography that develops around indentations. The results revealed that the topography is sensitive to the grain orientation, and the reproducibility of this method can be evaluated by determining the variation in indent topographies generated under nominally identical orientation conditions.

Lattice orientation characterization methods have recently received increased attention, owing to increased demand for improved understanding of the relationship between the micromechanical response and different crystallographic orientations. Traditional characterization techniques for determining the crystallographic properties of crystal samples include selected area electron diffraction (SAED) [19] and electron backscatter diffraction (EBSD) [13,20]. However, for polycrystalline systems with relatively small grains (e.g., recrystallized titanium alloys and ultrafine grains in shear bands) multiple sets of diffraction spots will occur in the SAED pattern, rendering further analysis difficult. The angular resolution of EBSD is usually larger than 0.5°, which is inadequate for investigating the small-scale deformation of grains. Moreover, for heavily deformed materials, the spatial resolution will be reduced to 100 nm [21,22], owing to the residual stress [23] and the resulting poor quality of the EBSD image. Therefore, SAED and EBSD are usually unsuitable for monitoring changes in deformed samples with ultrafine polycrystalline.

Precession electron diffraction (PED), a new method for orientation characterization similar to the ACOM-TEM technique, has emerged in recent years as a means of overcoming the drawbacks associated with EBSD measurements of fine grains [24,25]. The beam is taken off-axis by the upper deflection coils and precessed about the optic axis. Then the precessed beam is focused on the specimen, resulting in precessed and transmitted beams after diffraction. The lower deflection coils are used to descan the post-specimen precession, resulting in a diffraction pattern that is focused. Compared with EBSD patterns, these patterns are less sensitive to lattice distortions in highly deformed materials. PED can eliminate the dynamical effects of electron diffraction and obtain significant features such as crystal orientation and symmetry, so it is suitable for characterization of nanoscale and high-defect-density crystalline materials. For example, after conducting a PED analysis on nano-scale ultrafine grains generated in highly deformed regions of titanium alloy, Ghamarian [26] extracted maps of dislocation density with an ultimate spatial resolution of 1–2 nm. These maps were subsequently evaluated in order to understand deformation structure-microstructure correlations. Using PED combined with transmission electron microscopy (TEM) analysis, Mohseni [27] investigated the differences in microstructural evolution near grain or subgrain boundaries during solidification and wear. The results revealed that shear-strain-induced brittle fracture and shear bands lead to cracking in the case of nitride Ti–6Al–4V. In the case of nitride Ti–35Nb–7Zr–5Ta, strain-induced plastic deformation yielded an ultrafine tribolayer composed of both ultrafine β-Ti grains and larger α-Ti grains.

Unfortunately, contemporary experimental methods used to study the local mechanical response and orientation information are often limited by the test facilities, and the data acquired from the complex loading process is usually insufficient. The combination of a crystal plastic finite element method (CPFEM) and advanced experimental characterization methods has received significant attention as a means of overcoming this drawback. Through this combination, the microstructural evolution, mechanical responses, and deformation processes occurring under microscopic loads can be understood, tracked, and quantified, respectively. Unlike traditional finite element method (FEM), CPFEM (which is based on the crystal plasticity theory) considers plastic slip and lattice rotation as the only deformation mechanism. This method plays an important role in the investigation of the anisotropic mechanical properties characterizing single-crystal materials. Su et al. [18] used a combination of experimental measurements (including nano-indentation) and CPFEM for an in-situ study of deformation. The plastic-deformation sensitivity to the misorientation of the two grains was revealed by simulating the deformation near grain boundaries after indentation. The results also revealed that slip transfer across grain boundaries with poorly aligned slip systems is difficult, but the topographies are almost the same near small-angle grain boundaries. Demiral et al. [28] proposed an enhanced crystal plasticity model of the strain gradient, and revealed that this gradient can be used to characterize the deformation of a β-Ti alloy single crystal micro-pillar. The simulation predicted the size effect associated with an initial yield and the work hardening rate of small-scale components. The results revealed that the characteristic length-scale depends on the densities of and interaction between polar, statistical dislocations.

Table 1
Chemical composition of the as-received TC6 titanium alloy (wt%).

Al	Cr	Mo	Fe	Si	C	N	H	O	Ti
6	1.5	2.5	0.5	0.3	<0.07	<0.03	<0.01	<0.18	Bal.

Despite the aforementioned studies, the driving force for lattice rotation in local micro-regions subjected to complex loadings has rarely been investigated. Equiaxed or dual phase titanium alloys are composed of many primary α-phase grains, it is also because that α-phase of TC6 is with a relative higher elastic modulus but a relative lower yield strength than β-phase. The α-phase plays an important role in the macroscopic and microscopic mechanical responses of the material, and an investigation of the lattice rotation behaviors is essential for understanding/controlling these responses.

In this work, the lattice orientation after nano-indentation of a TC6 primary α-phase grain was determined through the focused ion beam (FIB) technique coupled with the PED. The obtained experimental results were compared with the CPFEM simulation results, which were calculated based on the code developed by our team. The nucleation and continuous growth process of subgrains were predicted by virtually tracking the misorientation angle map in three-dimensional (3D) space. Afterwards, the evolution of the slip-system types at typical local regions of the indentation was captured and discussed.

2. Material and experimental procedures

2.1. Sample preparation and initial lattice orientation characterization

The chemical composition of the as-received TC6 titanium alloy (Institute of Aeronautical Material, Beijing, China) is presented in Table 1.

A 6 mm × 4 mm × 1 mm specimen of the TC6 titanium alloy was obtained via wire electrical discharge machining. Afterward, the residual stress in the surface layers of the specimen was removed through mechanical polishing and electropolishing (25 °C, 25 V, 30 s, solution: 6% $HClO_4$, 34% $CH_3(CH_2)_3OH$, and 60% CH_3OH). A Nordlys Nano EBSD detector and the Oxford HKL Channel 5 system were used to characterize the two-phase microstructure and lattice orientation of the TC6 sample. The distribution of the primary α-phase grains and the initial orientation of each grain can be obtained from the resulting inverse pole figure (IPF) map (see Fig. 1(a)).

2.2. Nano-indentation in a primary α-phase grain

Indentation experiments were performed with a Berkovich indenter using a nano-indenter (MTS, Nano Indenter XP) with a constant force rate loading of 0.15 mN/s and a maximum load of 20 mN. Each indentation point was set in a 3 × 3 matrix with a horizontal and vertical spacing of 10 μm in the center of the sample surface.

The microstructure of the sample is characterized via EBSD. A single crystal grain with a unique initial orientation (Euler angles: 125.47°, 139.31°, 44.75°) is enclosed in the white dashed circle shown in the IPF map (see Fig. 1(a)). As shown in Fig. 1(b), the micromorphology of the indentation matrix was investigated via scanning electron microscopy (SEM), and the indentation lying completely in the selected primary α-phase grain was taken as the representative indentation. The α and β phases are clearly shown in Fig. 1(c), and (as previously stated) the indicated grain is a primary α-phase grain. Therefore, this indentation was selected for further experiments and simulations.

Subsequently, the corresponding surface topographies and the pile-up profiles were obtained through atomic force microscopy (AFM) scanning of the indented surfaces. Several 5 μm × 5 μm AFM images were taken and then analyzed (NanoScope Analysis V1.80, Bruker Corporation).

2.3. Lattice orientation of the slice across the indentation

The Helios NanoLab 600i FIB/SEM dual beam system was used to obtain a 5000 nm × 5000 nm × 50 nm slice, by cutting and lifting-out (with a focused Ga+ ion beam) along the center axis of the indentation. The voltage of Ga+ is 30 kV and the Pt deposition (with a thickness of ~0.1 μm) is used as a protection layer of the sample.

The lattice orientation of the slice was subsequently determined via high-resolution PED (step length: 7.8 nm) using a FEI Tecnai G2 F20 transmission electron microscope (at an accelerating voltage of 200 kV) with a NanoMEGAS SPINNING STAR system. A converged beam (diameter: ~1 nm) was precessed about the optic axis at an angle of 0.65° (PED step size: 7.8 nm). Afterword, the collected data was exported into a commercial software HKL CHANNEL5 (Oxford Instruments, Halifax Road, High Wycombe, BUCKS, HP12 3SE, UK) for analysis.

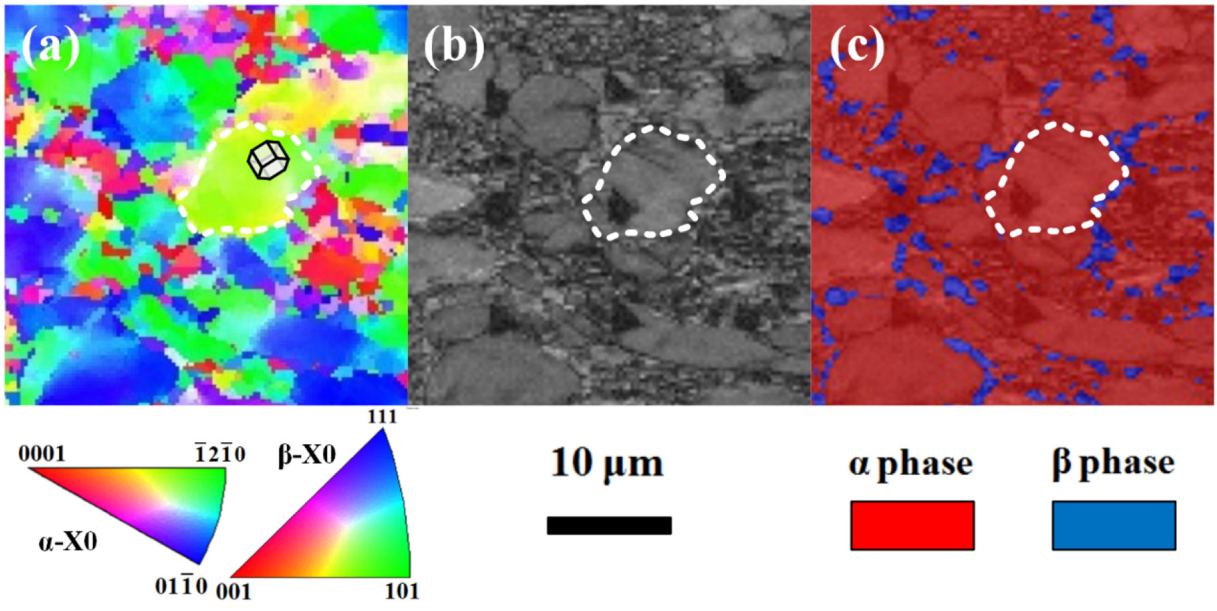

Fig. 1. Characterization of the sample: (a) IPF map before the indentation test; (b) SEM micrograph after the indentation test; (c) EBSD phase map.

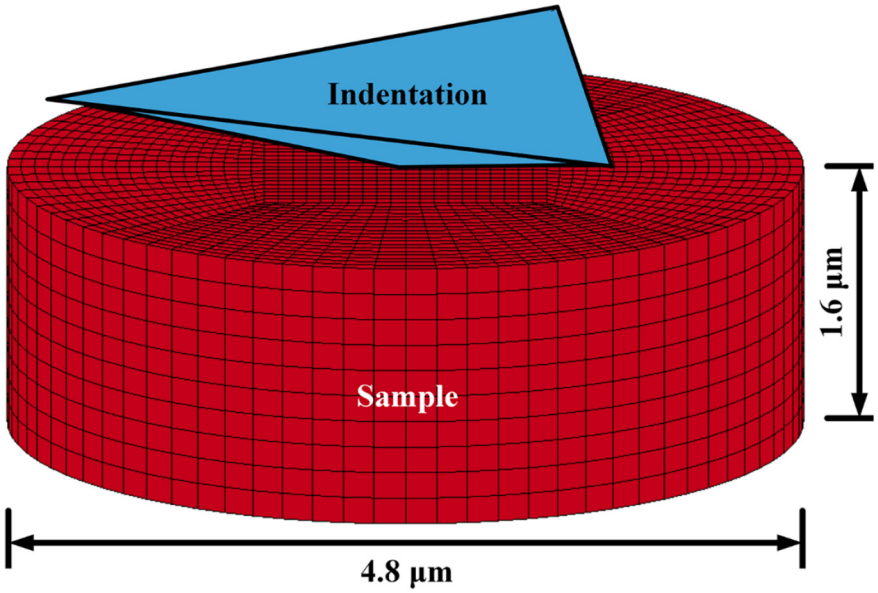

Fig. 2. 3D finite element model of nano-indentation.

3. Numerical simulation method

3.1. Finite element modeling and constitutive parameters

The 3D finite element model of the TC6 α-phase grain is shown in Fig. 2. The model size is Φ4.8 μm × 1.6 μm, and the bottom surface is fully constrained. The model is composed of hexahedral elements, with fine meshes in the center under the indenter and sparse meshes in the surrounding areas. Since the element size has a significant effect on the simulation results, models with different total number of elements will be discussed (see Section 4.1.1). Based on the EBSD results presented in Section 2.2, the elements of the model are all assigned the same initial lattice orientation as that of the primary α grain enclosed in the white dashed circle in Fig. 1(a). The non-reflective boundary is defined at the bottom and the surrounding side of the model, thereby describing the semi-infinite state of the sample.

As shown in Table 2, the elastic coefficient matrix parameters, the critical resolved shear stress (CRSS), and the hardening index of the TC6 primary α-phase are based on the previous work of our group [29]. These parameters are adjusted to optimized values by fitting the data of an in-situ tensile test (under a synchrotron radiation source) in the elastic-plastic self-consistent framework. In this way, the constitutive relations of each phase and parameters of the micro slip systems (such as CRSS values) were successfully obtained. Generally, the whole stress state of the specimen is complicated. It is under compression beneath the indentation, while other parts are in tensile state around the indentation. So the CRSS values obtained from a tensile test are used in present work, for the convenience of simulation.

CPFEM simulations, based on the program Microstructure-based Finite Element Simulation V1.0 developed by our research group [30], are performed in the current study. The crystal plastic constitutive parameters (see Table 2) are imported into the code. Afterward, the slipping mechanism is accounted for, in order to simulate the lattice orientation evolution of a single primary α-phase grain under the load of a Berkovich indenter. The simulation step is shown as follows:

(1) A parameter file that contains the elastic coefficient matrix parameters, CRSS, and hardening index of each typical slip system, and a parameter file containing the initial orientation information of each element are read into the system. The finite element model is then constructed in the sample coordinate system (SCS). The time-depth curve of the indenter is divided equally into 350 segments and each segment is used as the load curve for each substep of the simulation.

(2) The stress and strain increments of each element ($\Delta\sigma_{ij}$, $\Delta\varepsilon_{ij}$) can be obtained at each substep of nano-indentation loading. Accordingly, the Euler-angle increments can be calculated and added to the elements, thereby describing the rotation of the lattice and the newly updated orientation at different local micro-regions of the indentation.

(3) Each element in the model has an independent orientation after the Euler angles are updated, and the input intrinsic parameter is defined in the crystal coordinate system (CCS) of each grain. Therefore, a rotation matrix (with components calculated from the Euler angles) describing

Table 2
Crystal plastic constitutive parameters of the TC6 primary α-phase.

Density/g cm^{-3}	Poisson's ratio	C_{11}/GPa	C_{12}/GPa	C_{13}/GPa	C_{33}/GPa	C_{44}/GPa
4.4	0.3	168	97	77	198	43
Slip system		CRSS/GPa		τ_1/GPa	θ_0/GPa	θ_1/GPa
$\langle 11\bar{2}0\rangle\{0001\}$		0.33		0.13	0.115	0.021
$\langle 11\bar{2}0\rangle\{10\bar{1}0\}$		0.35				
$\langle 11\bar{2}0\rangle\{10\bar{1}1\}$		0.47				
$\langle 11\bar{2}3\rangle\{10\bar{1}1\}$		0.49				

the relationship between the SCS and the CCS is required. The transformation relationship between the crystal rotation matrix **g** and the Euler angles of the grain ($\varphi_1\ \Phi\ \varphi_2$) is given as follows:

$$\begin{aligned}\boldsymbol{g} &= \begin{bmatrix} cos\varphi_2 & sin\varphi_2 & 0 \\ -sin\varphi_2 & cos\varphi_2 & 0 \\ 0 & 0 & 1 \end{bmatrix}\begin{bmatrix} 1 & 0 & 0 \\ 0 & cos\Phi & sin\Phi \\ 0 & -sin\Phi & cos\Phi \end{bmatrix} \\ &\times \begin{bmatrix} cos\varphi_1 & sin\varphi_1 & 0 \\ -sin\varphi_1 & cos\varphi_1 & 0 \\ 0 & 0 & 1 \end{bmatrix} \\ &= \begin{bmatrix} cos\varphi_1\ cos\varphi_2 - sin\varphi_1\ sin\varphi_2 cos\Phi & sin\varphi_1\ cos\varphi_2 + cos\varphi_1\ sin\varphi_2 cos\Phi & sin\varphi_2 sin\Phi \\ -cos\varphi_1\ sin\varphi_2 - sin\varphi_1\ cos\varphi_2 cos\Phi & -sin\varphi_1\ sin\varphi_2 + cos\varphi_1\ cos\varphi_2 cos\Phi & cos\varphi_2 sin\Phi \\ sin\varphi_1 sin\Phi & -cos\varphi_1 sin\Phi & cos\Phi \end{bmatrix}\end{aligned} \tag{1}$$

(4) Through coordinate system transformation, the total stress $\Sigma\sigma_{cij}$ can be obtained from the sum of stress increments (the subscript c denotes the parameter in the CCS). The stress component of each slip system is calculated from $\tau_{RSS} = \sigma_{ij}\cdot cos\varphi_1 \cdot cos\varphi_2$, where φ_1 is the angle between $\Sigma\sigma_{cij}$ and the vector normal to the slip plane, and φ_2 is the angle between $\Sigma\sigma_{cij}$ and the slip direction.

(5) The Critical Resolved Shear Stress (CRSS, τ_0) of the slip system is used as a criterion for determining whether the slip system is activated. A $\tau_{RSS} > \tau_0$ indicates that slip systems are activated and plastic deformation occurs. When a slip system is activated, strain hardening occurs and the increment τ^i of the CRSS is related to the shear strain rate γ^j and the j-th slip system in the grain as follows:

$$\tau^i = \frac{d\tau^i(\Gamma)}{d\Gamma}\sum_j h^{ij}\gamma^j \tag{2}$$

where, Γ is the cumulative strain on the slip system and h_{ij} is the hardening coefficient associated with the system.

(6) In this simulation, plastic deformation is attributed to slip only. According to the Hill-Hutchinson polycrystal elastoplastic deformation theory, plastic strain results from the accumulative value of all slip system activations.

$$\boldsymbol{\varepsilon}_c^p = \sum_i \gamma^i \alpha^i \tag{3}$$

γ^i and α^i refer to the degree of the i-th slip system activation and the Schmid factor of the i-th slip system, respectively. In addition, Schmid factor is extremely difficult to calculate for an indentation test due to the non-uniaxiality of the stress, so Schmid factors in this work are calculated based on the orientation relationships of first principal stress and different slip systems of each element.

The state and orientation of each grain can be used to determine whether the grain is in the elastic phase or the plastic phase. The instantaneous stiffness matrix is then obtained, and the corresponding total stiffness coefficient matrix is calculated.

$$\boldsymbol{\sigma}_c = \begin{cases} \boldsymbol{L}_c^e \cdot \boldsymbol{\varepsilon}_c^e & (a) \\ \boldsymbol{L}_c^e \cdot \boldsymbol{\varepsilon}_c^e + \boldsymbol{L}_c^p \cdot \Sigma\gamma^i\alpha^i & (b) \end{cases} \tag{4}$$

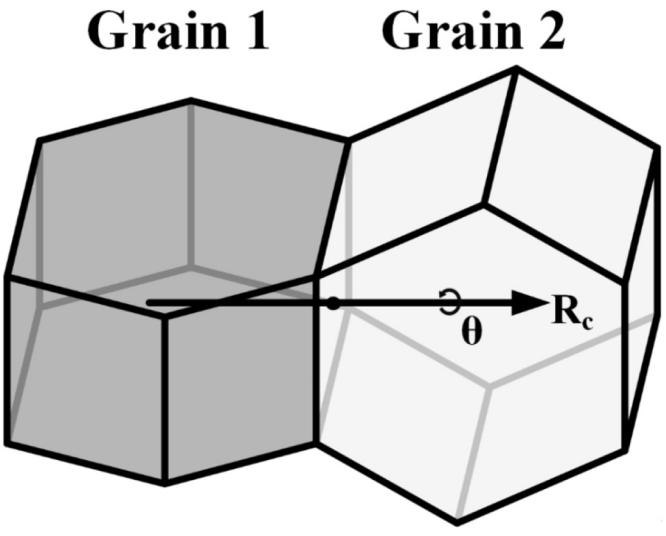

Fig. 3. Misorientation between two grains.

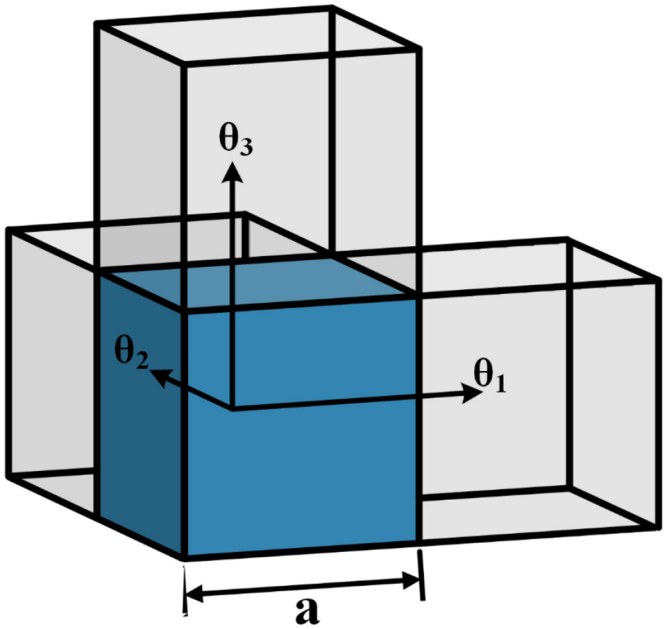

Fig. 4. GND calculation method based on average misorientation between the central voxel and the surrounding voxels.

where, **L** represents a matrix of stiffness coefficients, and subscripts e and p denote variables corresponding to the elastic phase and the plastic phase, respectively. Eq. (4b) shows that the stress σ is sum of elastic part and plastic part relating to different loading process, and each stress is the product of stiffness coefficients matrix L and strain ε.

(7) After the coordinate system transformation, the material constitutive parameters are updated and imported into the finite element model for the subsequent substep. These calculations are repeated until the entire nano-indentation loading process is completed.

3.2. Calculation of misorientation angle

The intragranular orientation changes caused by the accumulation of dislocations during plastic deformation may be characterized via the misorientation angle [31]. This angle increases with increasing material deformation and can be used to describe the different orientation relationships of the grains, as shown in Fig. 3.

The rotation axis R_c is selected as a common axis, and grain 1 is rotated around this common axis to the position of grain 2. As indicated in Fig. 3, the rotation angle corresponds to the misorientation angle θ. The matrix **M** [31] that embodies the misorientation between $\mathbf{G}_1$ and $\mathbf{G}_2$ is calculated from the orientations of grains 1 and 2 as follows:

$$\boldsymbol{M} = \boldsymbol{E}\boldsymbol{G}_1\boldsymbol{G}_2^{-1} = \boldsymbol{E}\boldsymbol{G}_1\boldsymbol{G}_2^{T} \tag{5}$$

where, $\mathbf{G}_2^{-1}$ is the inverse matrix of the rotation matrix $\mathbf{G}_2$, and **E** is the symmetric operation matrix related to the crystal symmetry. For the α-phase of the TC6 titanium alloy with hexagonal crystal symmetry, **E** is described by 12 equivalent expressions and, hence, **M** has multiple equivalent solutions. Generally, the **M** with the smallest difference in orientation is taken as the optimal solution from a series of equivalent solutions, and the corresponding misorientation angle θ [31] can be determined from:

$$\theta = \cos^{-1}\left\{\frac{\boldsymbol{M}_{11} + \boldsymbol{M}_{22} + \boldsymbol{M}_{33} - 1}{2}\right\} \tag{6}$$

3.3. Calculation of GND density

Physically, the dislocation density can be interpreted in terms of a low angle grain boundary model that accommodates a certain number of dislocation lines [32]. The spacing of several dislocation lines, average misorientation, and Burgers vector are denoted as d, θ_{av}, and b, respectively, where

Table 3
Dislocation types and weight factors of the TC6 primary α-phase [33–35].

Slip mode	Edge		Screw	
	Number	Weight	Number	Weight
$\langle 11\bar{2}0\rangle\{0001\}$	3	0.124	3	0.087
$\langle 11\bar{2}0\rangle\{10\bar{1}0\}$	3	0.124	0	–
$\langle 11\bar{2}0\rangle\{10\bar{1}1\}$	6	0.124	0	–
$\langle 11\bar{2}3\rangle\{10\bar{1}1\}$	12	0.437	6	0.306

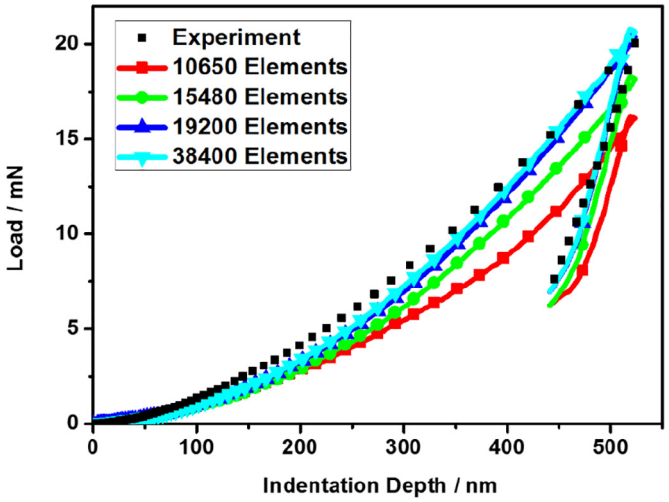

Fig. 5. Comparison of experimental and simulation results obtained for different numbers of total elements.

$1/d = \theta_{av}/|b|$. In the model shown in Fig. 4, a voxel with a side length a is taken as a research object. The average misorientation θ_{av} can be obtained from the misorientation angles θ_1, θ_2, and θ_3 between the adjacent voxels in each direction. The number of dislocation lines on a single surface is then determined from:

$$N = a^2\theta_{av}/|b| \tag{7}$$

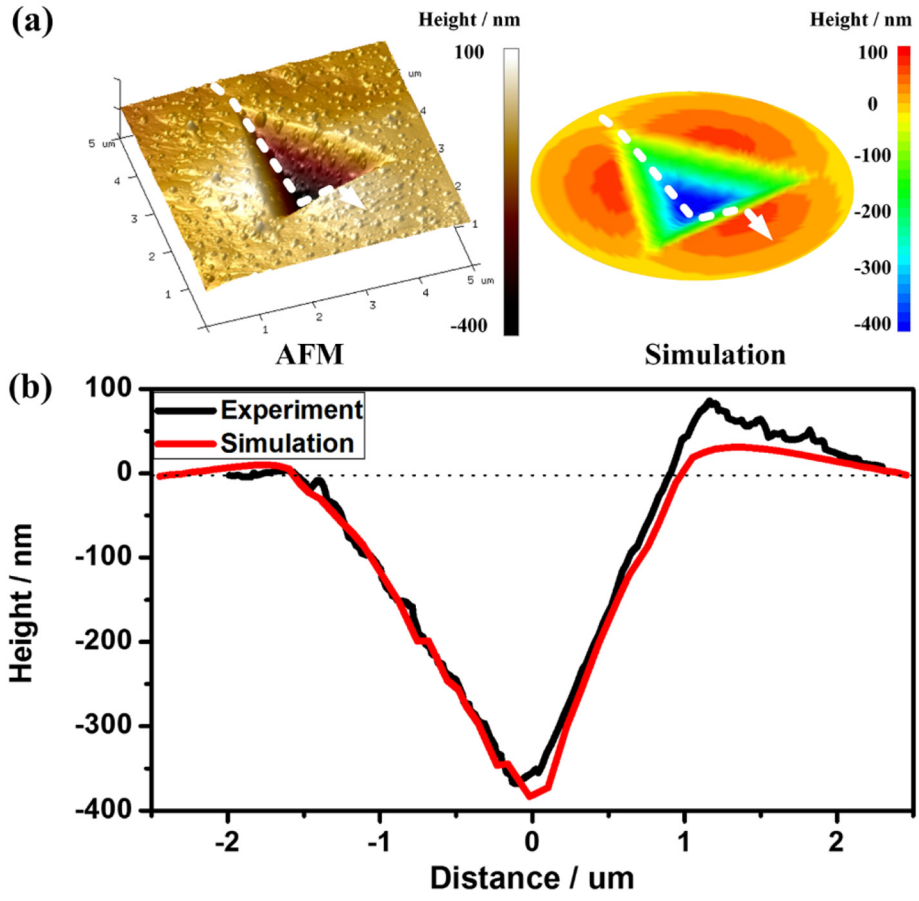

Fig. 6. Comparison of: (a) experimental and simulated morphologies of the indentation (b) height along the white arrows across the indentation.

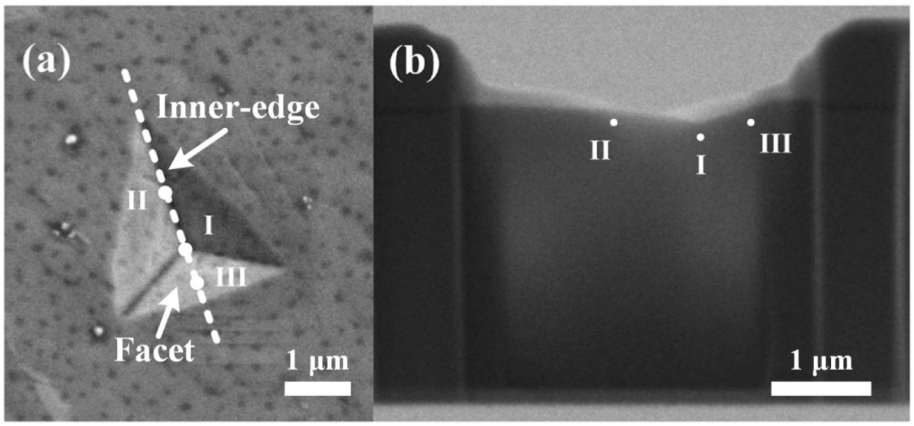

Fig. 7. (a) Morphology of the indentation, (b) slice cut by FIB.

In the 3D space, the target voxel shares the dislocation line of the six faces with the adjacent voxels and, hence, the dislocation density is given as follows [32]:

$$\rho_{total} = \frac{6}{2}\frac{a^2\theta_{av}}{|b|}\frac{1}{a^3} = \frac{3\theta_{av}}{|b|a} \tag{8}$$

Many types of dislocations occur in titanium alloys. Therefore, determining a unique GND density for different dislocation types associated with a given orientation difference is difficult. Different types of dislocations in the crystal have different energies and, hence, different effects on lattice distortion. In the calculations, these differences are reflected through a weight factor w. Burgers vector lengths of 2.95×10^{-10} m and 5.53×10^{-10} m have been reported for ⟨a⟩ type dislocations and ⟨c + a⟩ type dislocations, respectively, in α-phase titanium alloy (the weight factors corresponding to different types of dislocations are shown in Table 3).

The lowest energy criterion, which is used to determine the final GND, is given as follows:

$$L = \sum_{k=1}^{N}\left|\rho_{GND}^{k} w^{k}\right| \tag{9}$$

where, ρ_{GND}^{k} is the k-th GND density; w^k is the weight factor for the corresponding dislocation; N denotes all possible dislocation types [36,37]. Considering the lattice rotation gradient is much larger than the strain gradient, it is assumed that the strain gradient is negligible compared to the lattice rotation gradient in this work.

4. Results and discussion

4.1. Reliability analysis

4.1.1. Effect of mesh density on reliability

Different mesh densities are employed for the model. The simulated load between the indenter and the sample and the corresponding indentation depths are compared with the experimental values (see Fig. 5). Generally, large strain gradient or stress concentration during severe plastic deformation cannot be expressed precisely if using a low mesh density, due to the weakened stiffness matrix in the simulation. When the total number of elements is 10650 and 15480, the simulated maximum load values of the indenter are 16.16 N and 18.27 N, respectively, which are lower than the experimental value of 20.01 N. For 19200 and 38400 elements, the peak load values of the indenter are 20.46 N and 20.61 N, respectively, and the simulated curves and the experimental results exhibit the same trend. These two mesh densities yield a close correspondence between the calculated results and the experimental results, thereby demonstrating the reliability of the constitutive parameters associated with the TC6 primary α-phase. Since there is little improvement in the simulation with a denser mesh method, a mesh density of 38400 elements is adopted for the subsequent simulations.

4.1.2. Comparison of experimentally determined and simulated nanoindentation morphology

During the loading process, pile-up occurs around the indenter, owing to plastic deformation [38,39]. The pile-up patterns determined from the experimental and simulated indentation morphologies are compared in Fig. 6(a). The height of the pile-up can be obtained by taking the original surface height of the sample as the zero point. As the figure shows, the pile-up in the middle of the indentation boundaries is more significant than in the other regions. The AFM-determined and simulated height values along the symmetry axis, which is indicated by the white arrow in Fig. 6(a), are compared in Fig. 6(b). As the figure shows, the final indentation depth is 368.3 nm, which is smaller than the previously measured maximum depth of 513 nm. This indicates that after elastic-plastic deformation during the loading process, a 149.7 nm elastic rebound occurs in the subsequent unloading process. The height on the indentation inner-edge side (i.e., 6.16 nm) is slightly higher than the sample surface. However, on the indentation facet side, the sample undergoes plastic flow along the directions of the horizontal force, due to the significant plastic deformation caused by the indenter load. Therefore, the pile-up at the boundary of the facet (maximum height: 81.6 nm) is more significant than that of other regions. The numerical simulation results (depth of the indentation after the rebound: 383.5 nm, height of the pile-up on the inner-edge side: 9.94 nm) are consistent with the experimental results. Although the pile-up height on the facet side (i.e., 31.2 nm) is lower than the actual height (81.6 nm), the error falls in an acceptable range relative to the overall indentation depth. The close correspondence between the simulation results and the experimental results suggests that the constitutive parameters and the simulation method are quite reliable.

4.2. Evolution of lattice orientation and GND density in the slice

4.2.1. Orientation evolution in the slice

The lattice orientation of a nano-indentation sample is seldom determined via traditional EBSD. In this work, the orientation is determined via TEM. Prior to TEM analysis, the sample is examined via SEM (see Fig. 7(a)) and the selected symmetry axis across the indentation, and the facets as well as the inner-edges of the indentation are indicated. The slice shown in Fig. 7(b) is cut by FIB along the symmetry axis, and prepared for subsequent orientation analysis such as TEM and PED.

Elastic rebound will occur after nano-indentation and the lattice orientation is preserved during elastic deformation [40]. Therefore, in the

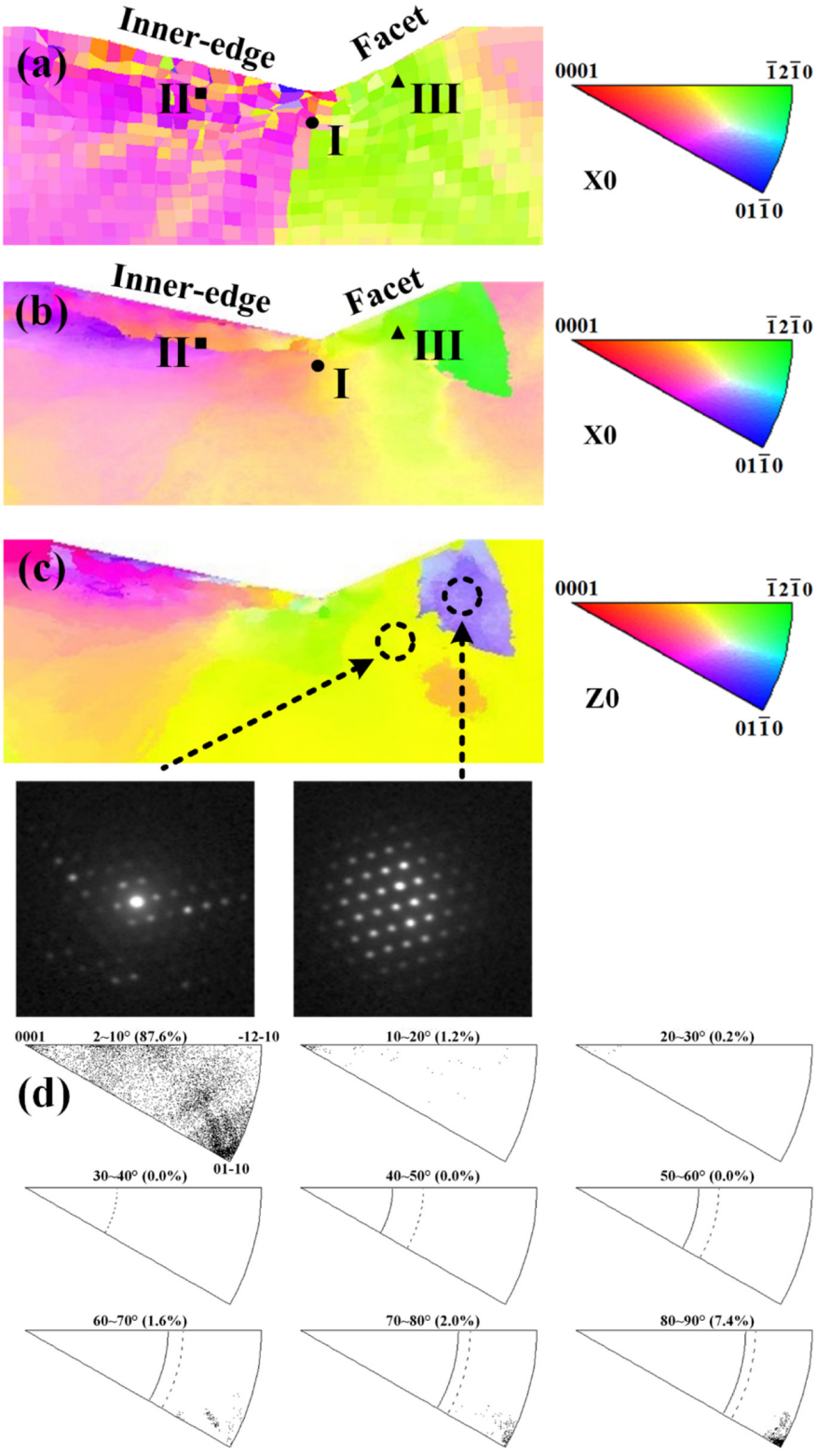

Fig. 8. IPF map of the slice after indentation: (a) simulation results along X, (b) experimental results along X, (c) experimental results along Z and diffraction patterns obtained from different subgrains, (d) distributions of rotation angles and rotation axes.

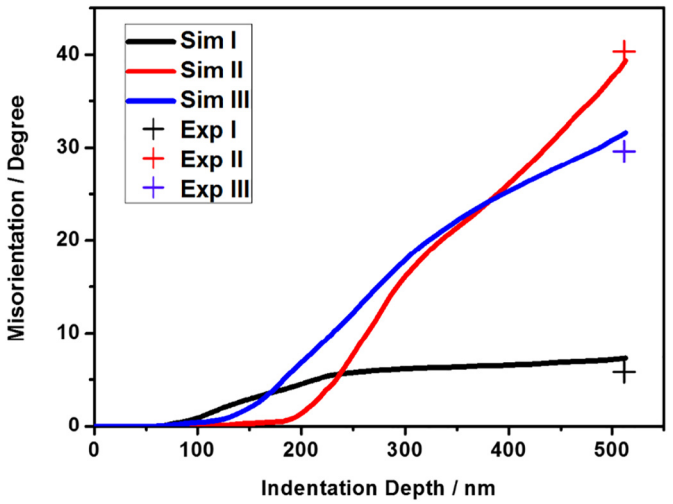

Fig. 9. Lattice rotation histories of selected elements under the indentation.

present study, the orientation evolution will be analyzed only during the loading process (0–513 nm). The mapping relationship between the lattice orientations and the IPF colors can be obtained from the IPF map generated by the Oxford HKL Channel 5 software, where the dictionary of Euler angles with the corresponding RGB values is established. A virtual IPF map can then be obtained based on the simulated orientation information and, the lattice orientation is illustrated. A high-resolution lattice orientation map (step size: 7.8 nm) was successfully obtained through PED in the slice beneath the indentation (despite the large residual stress caused by severe plastic deformation of the sample).

The experimentally determined IPF map and simulated IPF map are compared in Fig. 8. The predicted orientation gradient in the slice (see Fig. 8(a)) is clearly identifiable and acceptable, and corresponds quite closely to the experimentally determined gradient shown in Fig. 8(b). The good consistency between the simulation and experimental results indicates that the assumptions made in the simulation, such as CRSS values measured from a tensile test and negligence of strain gradient effect, are acceptable. Furthermore, the length scale effect in the current study has limited influence during the process, as reported in other CPFEM studies [18,41]. The lattice orientation located far beneath the indentation is considered the initial orientation. As Fig. 8(a) shows, the orientation of the lattice under the indentation inner-edge differs significantly from the orientation of the lattice under the indentation facet. The lattice under the indentation edge rotates to $\langle 01\bar{1}1\rangle$, whereas the lattice under the indentation facet rotates to $\langle \bar{1}2\bar{1}0\rangle$. However, the lattice orientation under the tip of the indenter changes only slightly from its initial orientation, as shown in the bottom region of Fig. 8(b). Fig. 8(c) shows the IPF map along Z axis and diffraction patterns measured from these micro-regions beneath the indentation by PED. The inhomogeneous intensity distribution observed in these diffraction patterns indicates that the corresponding micro-regions belong to different but adjacent subgrains, which further indicates the existence of subgrain boundaries formed by the accumulation of dislocations. Fig. 8(d) shows the distributions of rotation angles and rotation axes achieved by the Oxford HKL Channel 5 software. It can be figured out that 87.6% of the sub-grain boundaries have a misorientation angle of 2–10°, and there are no specific orientations of these rotation axes. The second most rotation angles (with a proportion of 7.4%) are focused in 80–90°, with a rotation axis of $\langle 01\bar{1}0\rangle$. Obviously, the main distributions of rotation angle and rotation axis are different from the typical deformation twins such as $85°\langle 11\bar{2}0\rangle$ or $65°\langle \bar{1}100\rangle$ [42]. So the subgrains are supposed to nucleate under the facets of the indentation, and then rotate continuously to different orientation.

Elements I, II, and III, which are under the tip of the indenter, under the indentation inner-edge, and under the indentation facet, respectively (see Fig. 8), are selected as the typical elements for further analyses. The misorientation angle at different indentation depths can be calculated based on the initial orientation of the lattice (see the details in Section 3.2). As the corresponding results in Fig. 9 show, Element I begins to rotate at an indentation depth of 60 nm, and the other two elements rotate only slightly. The lattice of Element III below the indention facet starts to rotate at a depth of 105 nm and the rotation degree is more significant than that of Element I. Subsequently, when the indenter is pressed down to 180 nm, Element II under the indentation inner-edge starts to rotate and the misorientation angle grows faster than those of the other elements. At depths larger than 400 nm, the misorientation angle of Element II exceeds that of Element III, suggesting that the maximum lattice rotation occurs under the indentation inner-edge. The simulation results show that the final misorientation angles of Elements I, II, and III are 6.15°, 39.36°, and 31.59°, respectively. These values are consistent with the PED results (i.e., 5.09°, 40.16°, and 29.05°, respectively) obtained at the same position. Different from the final distributions of lattice orientation achieved in other literatures [43,44], the specific rotation histories of these elements are also well captured by simulation. Description in detail contributes to further analysis of the grain rotation mechanism.

4.2.2. GND density analysis

The distribution and variation of the dislocation lines in the sample are closely correlated with the plastic deformation-induced evolution of the orientations. Fig. 10(a) shows an IPF map along Z of the slice, where different colors beneath the indentation indicate the lattice reorientation after plastic deformation. Based on the results of PED, the distribution of GND density can be further calculated via the method described in Section 3.3. Fig. 10(b) shows that the overall distribution

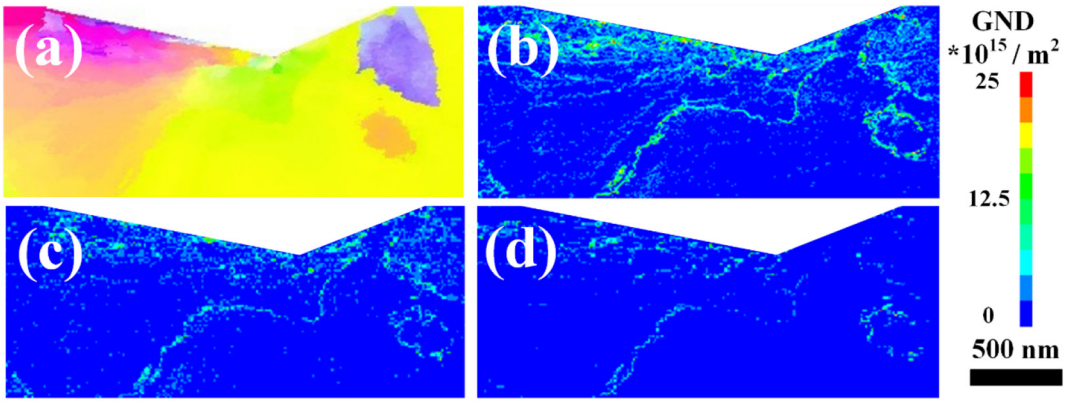

Fig. 10. (a) IPF map of a slice; and GND density calculated from the PED results (b) total (c) ⟨a⟩ type (d) ⟨c + a⟩ type.

of GND density is asymmetric around the indentation. Many dislocations (density: $1.58 \times 10^{16}/m^2$) accumulate under the indentation edge after loading. The density of dislocations is considerably higher than the densities occurring under the facet ($6.88 \times 10^{15}/m^2$) and below the tip of the indenter ($1.19 \times 10^{15}/m^2$). The contribution of different dislocation types is evaluated by dividing the GND into ⟨a⟩ type and ⟨c + a⟩ type dislocations (see Fig. 10(c) and (d), respectively, for the corresponding nephograms). As the figure shows, the ⟨a⟩ type dislocations in the sample far outnumber the ⟨c + a⟩ type dislocations. This results from the fact that, compared with the ⟨c + a⟩ type, the ⟨a⟩ type dislocations are activated relatively easily, i.e., with relatively lower dislocation energy and smaller critical shear stress, thereby playing a positive role in the coordinated deformation of the entire sample. Fewer ⟨c + a⟩ type dislocations are activated and, in contrast to the ⟨a⟩ type dislocations, are distributed under the indentation inner-edge. This is attributed to the fact that the stress beneath the indentation inner-edge is relatively higher (than at other regions) and the critical shear stress is easily reached. Therefore, during the entire loading process, more dislocations are activated beneath the inner-edges (than in other regions), resulting in more severe plastic deformation and, hence, larger misorientations, as illustrated in Fig. 9.

4.3. Analysis of 3D lattice rotations and slip-system activations

4.3.1. Subgrain generation and growth caused by lattice orientations

In addition to the lattice orientation on the 2D slice, the internal local orientation distribution of the entire sample can also be obtained (via CPFEM) in the 3D space. Fig. 11 shows a diagram where the surface orientation is rendered with the virtual 3D IPF map, misorientation angle, and elements (extracted from the FEM models) with misorientation angles >10°. Elements at indentation depths of 100 nm, 200 nm, 300 nm, 400 nm, and 500 nm are considered. With continuous loading and increase in the contact surface between the indenter and the sample, the area of lattice rotation expands gradually in the sample surface. Correspondingly, the rotating area is sub-divided into three parts (with quite different rotation directions) by the three inner-edges of the indenter. The lattice rotation increases with continued loading, and regions with large rotation are mainly distributed along the inner-edges. In addition, a maximum misorientation angle of ~40° occurs at an indentation depth of 500 nm, whereas the lattice rotation beneath the facet and tip of the indenter is relatively small.

Subgrain generation and growth can be further analyzed from Fig. 11. A misorientation angle >10° is generally considered essential for subgrain generation. Elements with such misorientations are, however, absent at indentation depths of 100 nm and 200 nm. When the indentation depth is 300 nm, three subgrains are nucleated under the facets of the indent, and the directions of lattice rotation become ⟨0001⟩, ⟨01$\bar{1}$1⟩, and ⟨$\bar{1}$2$\bar{1}$0⟩, respectively, due to the different load directions. With continued lattice rotation, the regions with rotations >10° become wider and deeper (compared with their original respective states), and merge with three different orientations when the indentation depth reaches 400 nm. Thereafter, the subgrains grow continuously and expand downward until an indentation depth of 500 nm is reached. This method predicts the generation of subgrains during nanoindentation successfully, which is consistent with the IPF maps and different misorientation angles of different elements.

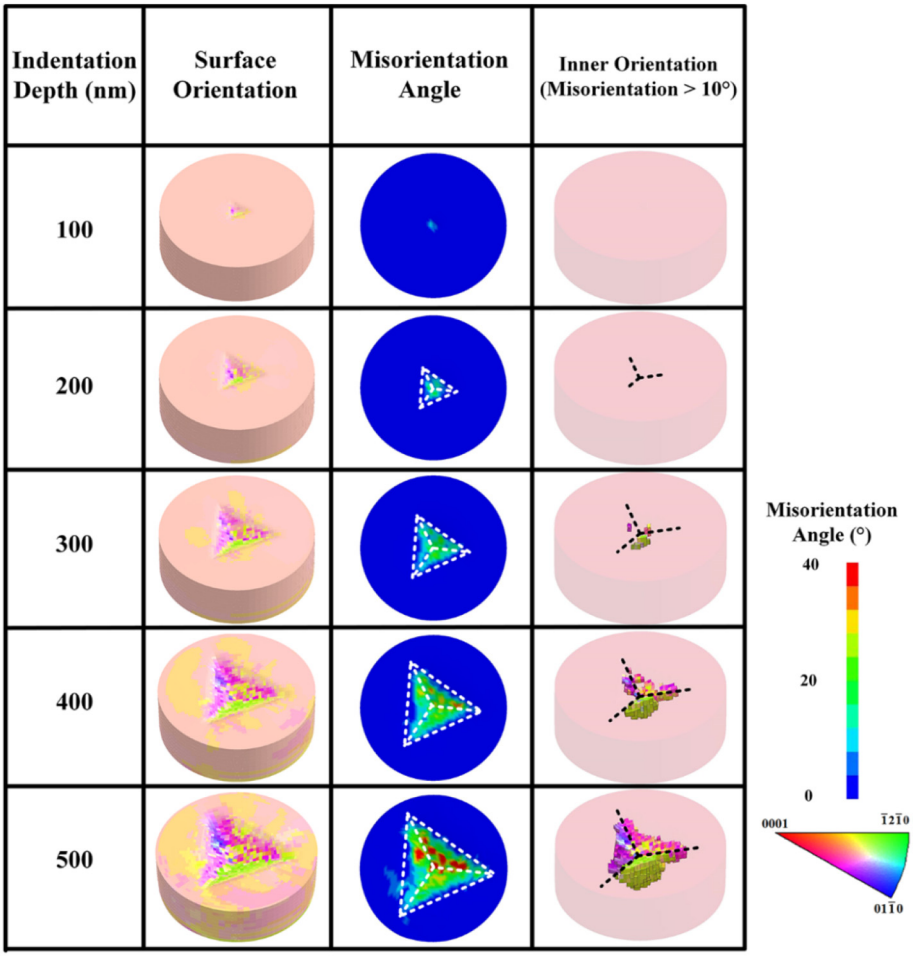

Fig. 11. Through-thickness distribution of the lattice orientation and elements with misorientation angles >10°.

4.3.2. Slip-system activation during loading

Subgrain generation at different locations during the loading process is elucidated by evaluating slip-system activation in the 3D model. Based on the method mentioned in Section 4.2.1, Element I, Element II, and Element III under the tip, inner-edge, and indentation facet, respectively, are selected as three typical elements for further analysis (see Fig. 12(a)). Fig. 12(b) shows the process of slip-system activation of the selected elements.

At an indenter depth of 100 nm, two slip systems, i.e., $(0001)[11\bar{2}0]$ and $(10\bar{1}0)[1\bar{2}10]$, are activated in Element I. These ⟨a⟩ type slip systems are easily activated as their slip directions are close to the local loading directions and the critical shear stresses are relatively small. Activation of the ⟨c + a⟩ type slip systems in Element I starts at an indentation depth of 200 nm. Three ⟨a⟩ and one ⟨c + a⟩ slip systems are activated, indicating that this element has undergone significant plastic deformation. Three ⟨a⟩ type slip systems are activated at depths of 300 nm and 400 nm. However, only two ⟨a⟩ type slip systems, i.e., $(01\bar{1}0)[\bar{2}110]$ and $(10\bar{1}1)[1\bar{2}10]$, are activated at a depth of 500 nm. This indicates that the generation of new dislocations in Element I is gradually reduced at the end of the indentation process, consistent with the distribution of the GND under the tip of the indenter (see Fig. 10(b)).

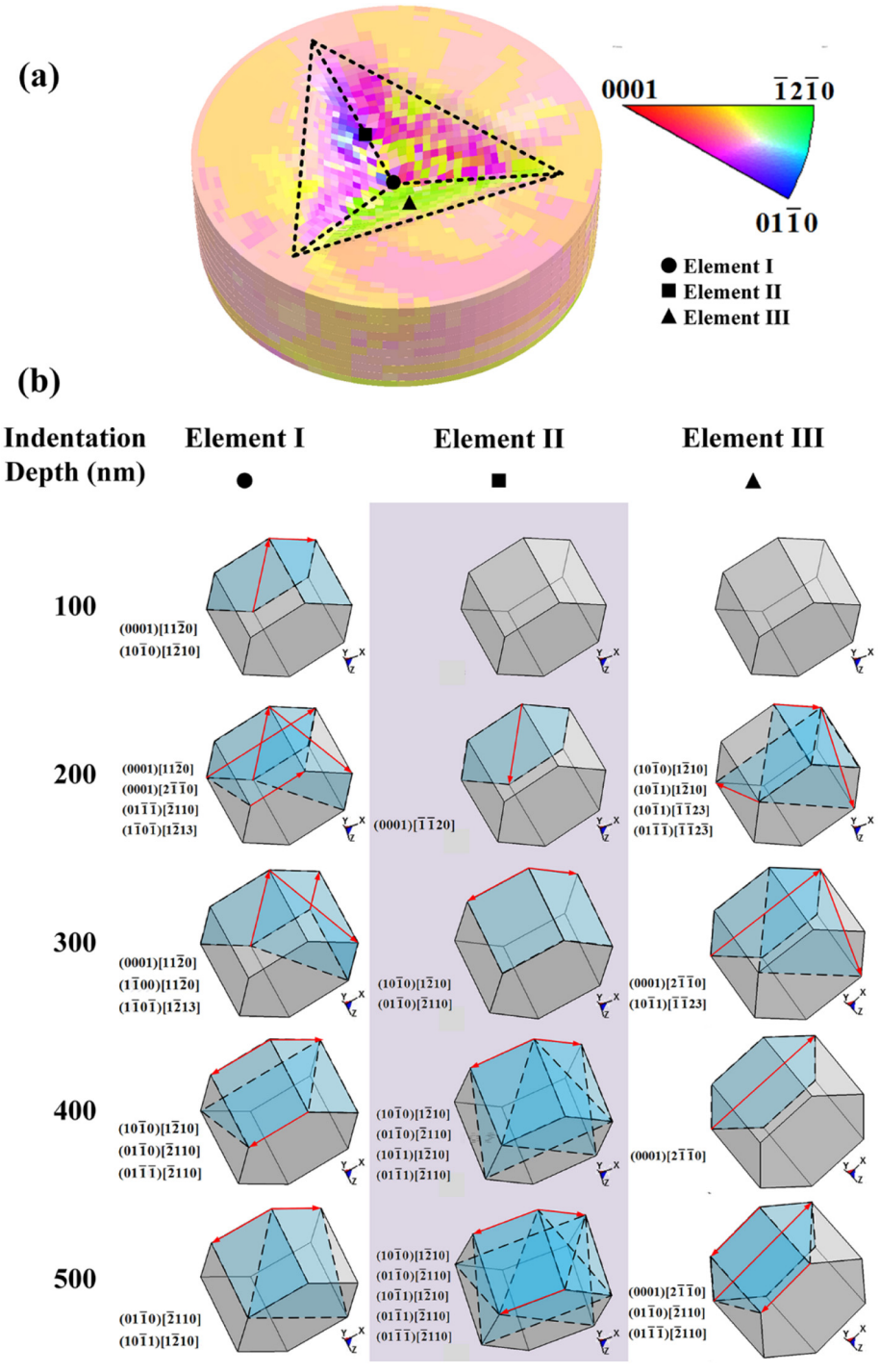

Fig. 12. (a) Relative positions on the sample surface at an indentation depth of 500 nm and (b) slip system activations during loading process of three typical elements.

At the beginning of the experiment employing an indentation depth of 100 nm, the contact between the indenter and Element II is slight and, hence, no slip system is activated in this element. When the indentation depth reaches 200 nm, only an ⟨a⟩ type dislocation, $(0001)[\bar{1}\bar{1}20]$, is activated, indicating that the plastic deformation is relatively slight. The number of activated slip systems in Element II increases significantly, however, with continued downward pressing of the indenter. Two slip systems, i.e., $(10\bar{1}0)[1\bar{2}10]$ and $(01\bar{1}0)[\bar{2}110]$, become activated at an indentation depth of 300 nm. Similarly, four and five slip systems are activated at depths of 400 nm and 500 nm, respectively. This dislocation-multiplication history in Element II is quite consistent with the corresponding rotation history obtained in Section 4.2.1.

As in the case of Element II, no slip system is activated in Element III at an indentation depth of 100 nm. Subsequently, due to the loading direction and the initial orientation of the element, four different types of slip systems are activated in Element III at an indentation depth of 200 nm. This results in complex plastic deformation behavior. However, during the subsequent loading process, slip-system activation is significantly reduced. Only one ⟨a⟩ type slip system, i.e., $(0001)[2\bar{1}\bar{1}0]$, is activated at an indentation depth of 400 nm, but the number of activated slip systems increases to three when the indenter is pressed to 500 nm. These results concur with those obtained for the lattice rotation history (see Section 4.2.1).

Although lattice rotations of these elements are different due to their independent loading conditions, it can be found that the number of activate slip systems has the same trend as the increasing of the misorientation angle, which is closely related to the generation of subgrains. This finding was verified in different micro-regions beneath the indentation. From the perspective of CPFEM simulated plastic deformation, the importance of slip system activation in subgrain generation is confirmed.

5. Conclusion

Although nano-indentation has become one of the most commonly applied methods of mechanical-property determination, the lattice rotation process in local micro-regions beneath the indentation and the underlying mechanism are quite complex. In this work, the nano-indentation-induced lattice rotation of a single α-phase grain in a TC6 titanium alloy is systematically investigated via a combination of experiments and in-house-developed program-assisted CPFEM simulations. Using PED combined with FIB allows high-resolution orientation characterization of the severely deformed Berkovich indentation, which is seldom achieved via traditional EBSD. It is found that subgrains are generated under the inner-edges and under the facet of the indentation, while the lattice directly under the tip of the indenter changes slightly from its initial orientation. Through the CPFEM simulation, this severe deformation is also successfully visualized by virtual IPF maps, revealing that the lattice directly beneath the tip of the indenter rotates first, but only slightly during the entire process. The greatest and the second-greatest lattice rotations occur under the indentation inner-edges and under the indentation facet, respectively. Moreover, the generation and growth of subgrains caused by the nano-indentation is virtually tracked by analyzing the lattice orientation in a 3D model. Three subgrains are nucleated under the facets of the indentation and then rotate to different directions. Thereafter, the subgrains grow continuously and expand downward with continued lattice rotation. Furthermore, the activation of different slip systems in the 3D model is numerically captured, which concur with those obtained for the lattice rotation history.

CRediT authorship contribution statement

Yu Zhou: Writing - original draft. **Qunbo Fan:** Conceptualization. **Xin Liu:** Methodology. **Duoduo Wang:** Investigation. **Xinjie Zhu:** Formal analysis.

Declaration of competing interest

There are no conflicts of interest.

Acknowledgement

We gratefully acknowledge the financial support from project 51571031 of the National Natural Science Foundation of China. Dr. Zheng from ZKKF (Beijing) Science & Technology Co., Ltd. is acknowledged for PED tests and GND analysis.

Appendix A. Supplementary data

Supplementary data to this article can be found online at https://doi.org/10.1016/j.matdes.2019.108423.

References

[1] C.H. Hager, J. Sanders, S. Sharma, A. Voevodin, Gross slip fretting wear of CrCN, TiAlN, Ni, and CuNiIn coatings on Ti6Al4V interfaces, Wear 263 (2007) 430–443.
[2] D. Banerjee, J.C. Williams, Perspectives on titanium science and technology, Acta Mater. 61 (2013) 844–879.
[3] F.P.E. Dunne, D. Rugg, A. Walker, Lengthscale-dependent, elastically anisotropic, physically-based hcp crystal plasticity: application to cold-dwell fatigue in Ti alloys, Int. J. Plast. 23 (2007) 1061–1083.
[4] M.A. Cuddihy, Z. Zheng, J. Gong, et al., Grain Size Effects in Hcp Polycrystals: From GNDs to Blocky Alpha, 2016.
[5] F.P.E. Dunne, A. Walker, D. Rugg, A systematic study of hcp crystal orientation and morphology effects in polycrystal deformation and fatigue, Proc. R. Soc. A-Math. Phys. Eng. Sci. 463 (2007) 1467–1489.
[6] L. Zeng, T.R. Bieler, Effects of working, heat treatment, and aging on microstructural evolution and crystallographic texture of alpha, alpha′, alpha″ and beta phases in Ti-6Al-4V wire, Mat. Sci. Eng. A-Struct. 392 (2005) 403–414.
[7] S. Roy, S. Suwas, Orientation dependent spheroidization response and macro-zone formation during sub beta-transus processing of Ti-6Al-4V alloy, Acta Mater. 134 (2017) 283–301.
[8] Z. Zhao, Q. Wang, J. Liu, et al., Effect of heat treatment on the crystallographic orientation evolution in a near-alpha titanium alloy Ti60, Acta Mater. 131 (2017) 305–314.
[9] Q. Wang, Z. Liu, Investigation the effect of strain history on crystallographic texture evolution based on the perspective of macro deformation for high speed machining Ti-6Al-4V, Mater. Charact. 131 (2017) 331–338.
[10] T.S. Jun, G. Sernicola, F.P.E. Dunne, et al., Local deformation mechanisms of two-phase Ti alloy, Mat. Sci. Eng. A-Struct. 649 (2016) 39–47.
[11] Z. Wang, Q. Li, Y. Li, Sliding of coherent twin boundaries, Nat. Commun. 8 (2017).
[12] Q. Pan, H. Zhou, Q. Lu, History-independent cyclic response of nanotwinned metals, Nature 551 (2017) 214.
[13] C. Fizanne-Michel, M. Cornen, P. Castany, et al., Determination of hardness and elastic modulus inverse pole figures of a polycrystalline commercially pure titanium by coupling nanoindentation and EBSD techniques, Mat. Sci. Eng. A-Struct. 613 (2014) 159–162.
[14] S. Ehtemam-Haghighi, G. Cao, L. Zhang, Nanoindentation study of mechanical properties of Ti based alloys with Fe and Ta additions, J. Alloy Compd. 692 (2017) 892–897.
[15] L. Wang, L. Xie, Y. Lv, et al., Microstructure evolution and superelastic behavior in Ti-35Nb-2Ta-3Zr alloy processed by friction stir processing, Acta Mater. 131 (2017) 499–510.
[16] Y. Lv, Z. Ding, J. Xue, et al., Deformation mechanisms in surface nano-crystallization of low elastic modulus Ti6Al4V/Zn composite during severe plastic deformation, Scr. Mater. 157 (2018) 142–147.
[17] T.S. Jun, D.E.J. Armstrong, T.B. Britton, A nanoindentation investigation of local strain rate sensitivity in dual-phase Ti alloys, J. Alloy Compd. 672 (2016) 282–291.
[18] Y. Su, C. Zambaldi, D. Mercier, et al., Quantifying deformation processes near grain boundaries in α titanium using nanoindentation and crystal plasticity modeling, Int. J. Plast. 86 (2016) 170–186.
[19] X. Sun, Y. Guo, Q. Wei, et al., A comparative study on the microstructure and mechanical behavior of titanium: ultrafine grain vs. coarse grain, Mat. Sci. Eng. A-Struct. 669 (2016) 226–245.
[20] D. He, J. Zhu, Z. Lai, et al., Residual elastic stress-strain field and geometrically necessary dislocation density distribution around nano-indentation in TA15 titanium alloy, T. Nonferr. Metal. Soc. 23 (2013) 7–13.
[21] S. Zaefferer, On the formation mechanisms, spatial resolution and intensity of back-scatter Kikuchi patterns, Ultramicroscopy 107 (2007) 254–266.
[22] X. Liu, N. Nuhfer, A. Rollett, et al., Interfacial orientation and misorientation relationships in nanolamellar Cu/Nb composites using transmission-electron-microscope-based orientation and phase mapping, Acta Mater. 64 (2014) 333–344.
[23] F.J. Humphreys, Y. Huang, I. Brough, et al., Electron backscatter diffraction of grain and subgrain structures - resolution considerations, Journal Of Microscopy-Oxford 195 (1999) 212–216.
[24] U. Santiago, J.J. Velázquez-Salazar, J.E. Sanchez, et al., A stable multiply twinned decahedral gold nanoparticle with a barrel-like shape, Surf. Sci. 644 (2016) 80–85.

[25] E.F. Rauch, M. Veron, Automated crystal orientation and phase mapping in TEM, Mater. Charact. 98 (2014) 1–9.
[26] I. Ghamarian, Y. Liu, P. Samimi, et al., Development and application of a novel precession electron diffraction technique to quantify and map deformation structures in highly deformed materials-as applied to ultrafine-grained titanium, Acta Mater. 79 (2014) 203–215.
[27] H. Mohseni, P. Nandwana, A. Tsoi, et al., In situ nitrided titanium alloys: microstructural evolution during solidification and wear, Acta Mater. 83 (2015) 61–74.
[28] M. Demiral, K. Nowag, A. Roy, et al., Enhanced gradient crystal-plasticity study of size effects in a beta-titanium alloy, Model. Simul. Mater. Sc. 25 (2017).
[29] R. Shi, G. Li, Q. Fan, et al., Determination of the single-phase constitutive relations of α/β dual phase TC6 titanium alloy, Mat. Sci. Eng. A-Struct. 675 (2016) 138–146.
[30] G. Li, 3D complex Microstructure Model Construction and Static/Dynamic Mechanical Behavior Simulation of TC6 Titanium Alloy, [D], Beijing Institute of Technology, 2017.
[31] E. Olaf, R. Valerie, Introduction to Texture Analysis Macrotexture, Microtexture, and Orientation Mapping, CRC Press, FL, USA, 2009 40–42.
[32] P.J. Konijnenberg, S. Zaefferer, D. Raabe, Assessment of geometrically necessary dislocation levels derived by 3D EBSD, Acta Mater. 99 (2015) 402–414.
[33] S. Zaefferer, A study of active deformation systems in titanium alloys: dependence on alloy composition and correlation with deformation texture, Mat. Sci. Eng. A-Struct. 344 (2003) 20–30.
[34] D. He, J. Zhu, Z. Lai, et al., Residual elastic stress-strain field and geometrically necessary dislocation density distribution around nano-indentation in TA15 titanium alloy, Trans. Nonferrous Met. Soc. China 23 (2013) 7–13.
[35] T.B. Britton, H. Liang, F.P.E. Dunne, et al., The effect of crystal orientation on the indentation response of commercially pure titanium: experiments and simulations, P. Roy. Soc. A: Math. Phy. 466 (2010) 695–719.
[36] A. Arsenlis, D.M. Parks, Crystallographic aspects of geometrically- necessary and statistically-stored dislocation density, Acta Mater. 47 (1999) 1597–1611.
[37] S. Sun, B.L. Adams, W.E. King, Observations of lattice curvature near the interface of a deformed aluminium bicrystal, Philosophical Magazine A 80 (2000) 9–25.
[38] P. Clement, S. Meille, J. Chevalier, et al., Mechanical characterization of highly porous inorganic solids materials by instrumented micro-indentation, Acta Mater. 61 (2013) 6649–6660.
[39] V. Karthik, P. Visweswaran, A. Bhushan, et al., Finite element analysis of spherical indentation to study pile-up/sink-in phenomena in steels and experimental validation, Int. J. Mech. Sci. 54 (2012) 74–83.
[40] L. Margulies, G. Winther, H.F. Poulsen, In situ measurement of grain rotation during deformation of polycrystals, Science 291 (2001) 2392–2394.
[41] J.W. Kysar, Y. Saito, M.S. Oztop, Experimental lower bounds on geometrically necessary dislocation density, Int. J. Plast. 26 (2010) 1097–1123.
[42] L. Nervo, A. King, A. Fitzner, et al., A study of deformation twinning in a titanium alloy by X-ray diffraction contrast tomography, Acta Mater. 105 (2016) 417–428.
[43] C. Reuber, P. Eisenlohr, F. Roters, Dislocation density distribution around an indent in single-crystalline nickel: comparing nonlocal crystal plasticity finite-element predictions with experiments, Acta Mater. 71 (2014) 333–348.
[44] T.J. Ruggles, D.T. Fullwood, J.W. Kysar, Resolving geometrically necessary dislocation density onto individual dislocation types using EBSD-based continuum dislocation microscopy, Int. J. Plast. 76 (2016) 231–243.